Marrying SPR excitation and metal-support interactions

Nanoscale

Accepted Manuscript

This article can be cited before page numbers have been issued, to do this please use: R. D. S. Geonmonond, J. Quiroz, G. D. F. S. R. Rocha, F. E. Oropeza, C. D. J. Rangel, T. S. Rodrigues, J. P. P. Hofmann, E. J.M. Hensen, R. A. Ando and P. Camargo, *Nanoscale*, 2018, DOI: 10.1039/C8NR00934A.

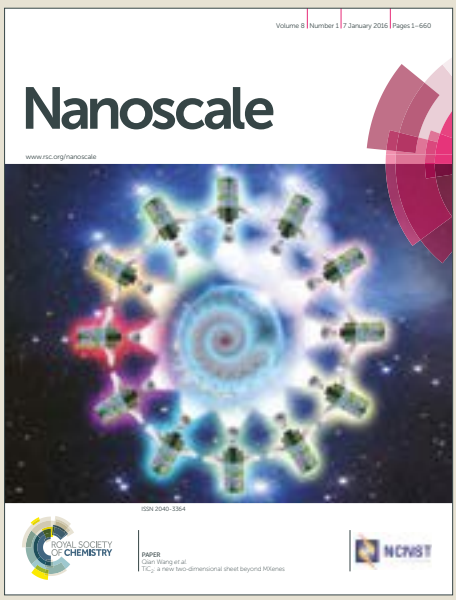

ROYAL SOCIETY OF CHEMISTRY

rsc.li/nanoscale

Marrying SPR Excitation and Metal-Support Interactions: Unraveling the Contribution of Active Surface Species in Plasmonic Catalysis

Rafael S. Geonmonond[a], Jhon Quiroz[a], Guilherme F. S. R. Rocha[a], Freddy E. Oropeza[b], Clara J. Rangel[a], Thenner S. Rodrigues[c], Jan P. Hofmann[b], Emiel J. M. Hensen[b], Rômulo A. Ando[a], and Pedro H. C. Camargo[a*]

[a]*Departamento de Química Fundamental, Instituto de Química, Universidade de São Paulo Av. Prof. Lineu Prestes, 748, 05508-000, São Paulo-SP, Brazil*

[b] *Laboratory of Inorganic Materials Chemistry, Department of Chemical Engineering and Chemistry, Eindhoven University of Technology, P.O. Box 513, 5600 MB Eindhoven, The Netherlands*

[c] *Instituto de Pesquisas Energéticas e Nucleares, IPEN-CNEN, 05508-000, São Paulo-SP, Brazil*

**Corresponding author. E-mail: camargo@iq.usp.br*

View Article Online
DOI: 10.1039/C8NR00934A

ABSTRACT

Plasmonic catalysis takes advantage of the surface plasmon resonance (SPR) excitation to drive or accelerate chemical transformations. In addition to the plasmonic component, the control over metal-support interactions in these catalysts is expected to strongly influence the performances. For example, CeO_2 has been widely employed towards oxidation reactions due to its oxygen mobility and storage properties, which allow for the formation of Ce^{3+} sites and adsorbed oxygen species from metal-support interactions. It is anticipated that these species may be activated by the SPR excitation and contribute to the catalytic activity of the material. Thus, a clear understanding of the role played by the SPR-mediated activation of surface oxide species at the metal-support interface is needed in order to take advantage of this phenomenon. Herein, we describe and quantify the contribution from active surface oxide species at the metal-support interface (relative to O_2 from air) over the activities in green SPR-mediated oxidation reactions. We employed CeO_2 decorated with Au NPs (Au/CeO_2) as a model plasmonic catalyst and the oxidation of p-aminothiophenol (PATP) and aniline as proof-of-concept transformations. We compared the results with SiO_2 decorated with Au NPs (Au/SiO_2), in which the formation of surface oxide species at the metal-support interface is not expected. We found that the SPR-mediated activation of surface oxide species at the metal-support interface in Au/CeO_2 played pivotal role to the detected activities, being even higher than the contribution coming from the activation of O_2 from air.

View Article Online
DOI: 10.1039/C8NR00934A

INTRODUCTION

Plasmonic catalysis takes advantage of the localized surface plasmon resonance (SPR) excitation to accelerate or mediate chemical reactions.[1–3] Recently, this field has attracted much attention due to the possibility of harvesting solar light as an energy input to drive a range of chemical transformations.[4–11] This can be accomplished, for example, by the utilization of metal nanoparticles as catalysts possessing strong SPR in the visible or near-infrared range, which include gold (Au), silver (Ag), and copper (Cu) nanoparticles (NPs).[12–14] Hence, plasmonic catalysis is expected to contribute towards the development of green (or greener) catalysis, which remain challenging in terms of both activity and selectivity.[15] Among green transformations, light-assisted oxidations using air or molecular oxygen (O_2) as the oxidant represents an interesting example, as it has been shown that the SPR excited hot electrons can efficiently activate molecular oxygen.[16–19]

In addition to the metal nanoparticles or active phase, it is well-established that optimizing metal-support interactions is an efficient strategy to the improvement of performances in nanocatalysis.[20,21] Among the several supports, CeO_2 has been widely employed in oxidation reactions due to its oxygen mobility and storage properties, which can be further enhanced at the metal-support interface due to metal-support interactions.[22] In this case, the formation of Ce^{3+} as well as adsorbed oxygen species (O^{2-} or O^-) have been described. In the context of plasmonic catalysis, these species may be activated by the SPR excitation as a result of metal-support interactions and contribute to the optimization of catalytic activities towards oxidation reactions.[23,24]

In order to take advantage of this phenomenon, a clear understanding on the role played by the SPR-mediated activation of surface oxide species at the metal-support interface

View Article Online
DOI: 10.1039/C8NR00934A

relative to the contribution/activation of O_2 from air is required. In this paper, we describe a relatively simple approach that enabled us to systematically isolate and quantify the contribution from surface oxide species at the metal-support interface (relative to O_2 from air) over the activities in green SPR-mediated oxidation reactions. We employed CeO_2 decorated with Au NPs (Au/CeO_2) as a model plasmonic material and the oxidation of *p*-aminothiophenol (PATP) and aniline as proof-of-concept transformations. We performed a series of control experiments and compared the results with SiO_2 decorated with Au NPs (Au/SiO_2), in which the formation of active surface oxide species at the metal-support interface is not expected. We found that the SPR-mediated activation of surface oxide species at the metal-support interface in Au/CeO_2 played a major role to the detected activities, being even higher than the contribution coming from the activation of O_2 from air.

RESULTS AND DISCUSSION

Scanning electron microscopy (SEM) images, ultraviolet-visible (UV-Vis) spectrum, and the histogram of size distribution for the Au NPs employed for the synthesis of Au/CeO_2 and Au/SiO_2 materials are shown in Figure S1A-C. The Au NPs were 22 nm ± 3 nm in diameter, displayed spherical shape, relatively monodisperse sizes, and a well-defined surface plasmon resonance (SPR) band centered at 525 nm assigned to the dipolar SPR mode.[25] Au NPs were incorporated onto CeO_2 and SiO_2 in order to produce Au/oxide solid catalysts. This not only facilitates applications in SPR-mediated catalysis both in gas or liquid phase, but also opens the possibility to enable further improvements in activity via metal-support interactions, as we describe below. For example, the deposition of Au NPs over CeO_2 surface improved the performance of Au/CeO_2 catalyst over the CO oxidation reaction at low temperatures.[26]

View Article Online
DOI: 10.1039/C8NR00934A

Figure 1A and B shows SEM and TEM images of the obtained Au/CeO_2 and Au/SiO_2 materials, respectively. The images show that for both samples a homogeneous distribution of Au NPs over the oxide surfaces without significant agglomeration or changes in shape and size was obtained using the preparation method described below. Figure S2 shows the histograms of size distribution or Au NPs in both Au/CeO_2 and Au/SiO_2 materials. It can be observed that the Au NPs had similar sizes on both supports, corresponding to 21.8 ± 3.1 and 21.9 ± 3.2 nm in diameter for Au/SiO_2 and Au/CeO_2, respectively. Additionally, the Au weight percentage (wt%) as determined by flame atomic absorption spectroscopy (FAAS) was to 4.9 for Au/CeO_2 and 4.2 for Au/SiO_2, which indicates our incipient wetness impregnation method enabled the deposition of Au NPs in high yields and without loss of morphology.

The Au/CeO_2 and Au/SiO_2 materials (and CeO_2 and SiO_2 the supports) were analyzed by diffuse reflectance spectroscopy (DRS) and X-ray powder diffraction (XRD) as shown in Figures 1C and D, respectively. The diffuse reflectance spectra for Au/CeO_2 and Au/SiO_2 (solid and dashed red traces, respectively) indicate the appearance of a broad band at 500-550 nm assigned to the Au SPR excitation, which resembles the spectra obtained for Au NPs as shown in Figure S1. This signal was not present in the individual CeO_2 and SiO_2 supports (solid and dashed black traces, respectively). XRD patterns (Figure 1D) showed that CeO_2 displayed a cubic Fm-3m structure (ICSD collection code 28753)[27] and SiO_2 presented the hexagonal P_{3221} structure (ICSD collection code 071396)[28] (black traces). The XRD data indicates that no significant crystalline impurities were present in the materials. While the peak associated to (111) reflection of *fcc* Au nanospheres in 38.5° was clearly detected in Au/SiO_2, its relative intensity was much smaller in Au/CeO_2. The relative low intensity of the SiO_2 XRD pattern facilitate the observation of the reflection associated to *fcc* Au, namely (111) at 38.5, (200) at 44.2, (220) at 64.4 and (311) at 77.3. The high intensity of the CeO_2 XRD pattern, associated

View Article Online
DOI: 10.1039/C8NR00934A

with the larger atomic number of Ce, obscures most of the reflection of the Au NPs in the XRD pattern of the Au/CeO_2 sample. However, the Au (111) can be clearly detected and we can confirm the FWHM of the peak is similar to the Au (111) refection in the Au/SiO_2 sample (Figure S3). It is important to note that the Au loading and particle size distribution were similar in both samples as shown by FAAS and SEM/TEM.

It is well-established that the presence of Au NPs contribute to the reduction of surface CeO_2 layers, favoring the O_2 mobility and the presence of oxygen species at the interface as a result of metal-support interactions.[30] In order to probe this effect, we performed temperature-programmed reduction with hydrogen (H_2-TPR) experiments for both CeO_2 and Au/CeO_2 materials as shown in Figure 2A (black and red traces, respectively). The H_2-TPR profile of CeO_2 was characterized by the presence of two reduction peaks: the peak at temperatures between 500-650 ^oC associated to the reduction of non-stoichiometric oxides of composition Ce_yO_x at the surface[31] and the peak centered at 940 ^oC is ascribed to the reduction of CeO_2 to Ce_2O_3.[32,33] In Au/CeO_2, it can be observed that the presence of Au lowered the temperature for the reduction of Ce_yO_x oxides at the surface (this peak shifted from 620 to 410^oC). This agrees with a significant metal-support interaction due to Au deposition.[31] Interestingly, the H_2-TPR profile for SiO_2 is characterized by a single peak assigned to the bulk SiO_2 reduction (SiO_2 does not display the same surface oxygen mobility properties as compared to CeO_2, Figure S4A). In both materials, no peaks related to the reduction of Au were observed (as expected for Au^0).

The strong metal-support interactions and oxygen vacancy properties in CeO_2 and Au/CeO_2 were further characterized by Raman spectroscopy (Figure 2B, black and red traces, respectively). It is noteworthy that oxygen vacancies are structural defects that can adsorb O_2 molecules and are intimately related to oxygen mobility and storage capacity [34]. The Raman

View Article Online
DOI: 10.1039/C8NR00934A

spectra for Au/CeO_2 and CeO_2 presented similar profiles in terms of band intensity and position. The strong band centered at 467 cm^{-1} can be attributed to the symmetric stretching vibration mode of oxygen atoms around the Ce^{4+} ions.[35,36] In addition, the Raman mode near 625 cm^{-1}, corresponding to the presence of oxygen vacancies, can be observed in the Au/CeO_2 material.[36,37] Moreover, it is well known that the presence of Ce^{3+} is correlated with the generation of oxygen vacancies in order to maintain the electrostatic balance of the lattice.[38] The Ce 3d core levels XPS spectra show peak positions characteristic of CeO_2[39] with the presence of Ce^{3+} in both CeO_2 and Au/CeO_2 samples (Figure S5A). Moreover, the photoemission spectrum of Au/CeO_2 in the Au 4f region (Figure S5B) showed two intense photoelectron peaks with maximum at binding energy (BE) values of 83.8 e 87.4 eV ascribed to the Au $4f_{7/2}$ and $4f_{5/2}$ doublet, respectively. These BE values are characteristics of Au species in the metallic state,[40] in agreement with the XRD and H_2-TPR.

Figure 2C and D depict the XPS spectra for the O1s region for CeO_2 and Au/CeO_2 samples, respectively. The signal was deconvoluted into three components located at 530, 531 and 533 eV (Table S1). These are assigned to lattice oxygen (O_L), oxygen vacancies or surface oxygen ions (O_S), and adsorbed water (O_W), respectively.[41] It can be observed that, for both samples, the signal from O_L had the highest intensity, contributing with 68% and 53% of the signal detected for CeO_2 and Au/CeO_2, respectively. In Au/CeO_2, the decrease of the O_L contribution was directly associated with an increase of the O_S contribution. In fact, it increased from 29% in CeO_2 to 46% in Au/CeO_2. The O_S/O_L ratio (Table S1), also confirms that the O_S/O_L ratio was higher for Au/CeO_2 sample. These results suggest that more surface adsorbed oxygen species (O^{2-} or O^-), or oxygen vacancies and defects have been created on the cerium oxide after the Au NPs addition as a result of metal-support interactions in this

system. The XPS spectra for the O1s and Au4f core-level regions of SiO_2 and Au/SiO_2 are shown in Figure S4C and D.

After the morphological, electronic, and chemical characterization of the obtained Au/CeO_2 material, we turned our attention to the investigation of the SPR-mediated catalytic activities. We were particularly interested in probing and isolating the effect of the activated oxygen species at the metal-support interface over the plasmonic catalytic activities. In Au/CeO_2 materials, reactive O_2 species that arise from metal-support interactions can be present as superoxo (O_2^-), peroxo (O_2^{2-}), or dissociated (2x O^{2-}) forms, which contribute to the detected superficial oxygen signals detected by XPS.[42] Thus, it is highly anticipated that these species are expected to play a key role in oxidation reactions promoted by heterogeneous catalysts, in photocatalysis and/or SPR-mediated catalysis.

In order to address this challenge, our approach consisted on probing the plasmonic catalytic activity employing a transformation that relies on the activation of O_2 via SPR excitation. Specifically, this can be achieved by: *i*) comparing the performances of Au/CeO_2 (in which the SPR excitation can activate oxygen species from both metal-support interactions and from O_2 atmosphere) relative to Au/SiO_2 (in which SPR excitation can activate only atmospheric O_2 due the absence of active oxygen species originating from metal-support interactions) as depicted Figure 3; and *ii*) probing the performances of Au/CeO_2 in the absence of O_2 atmosphere.

We started by employing the SPR-mediated oxidation of *p*-aminothiophenol (PATP) to *p,p'*-dimercaptoazobenzene (DMAB) by activated O_2 as a model reaction according to the following equation:

$$2AuS\text{-}Ph\text{-}NH_2 + {}^3O_2 + h\nu \rightarrow AuS\text{-}Ph\text{-}N{=}N\text{-}Ph\text{-}SAu + 2H_2O \qquad (1)$$

View Article Online
DOI: 10.1039/C8NR00934A

In this transformation, SPR excitation in Au NPs can lead to the formation of hot electrons, i.e., electrons that occupy energy states above the Fermi level during plasmon oscillation.[43,44] Under appropriate conditions, these hot electrons can trigger charge transfer processes at the metal-molecule interface and thus mediate the oxidation or reduction transformations.[45,46] In the context of the SPR-mediated PATP oxidation, hot electrons produced from SPR-excited Au NPs can be transferred to adsorbed O_2 molecules (from air), which are activated to $^2O_2^-$ ions, which subsequently contribute to the DMAB formation at the metal surface.[47,48,49,50]

The laser-power-dependent spectra employing 632.8 nm as the excitation wavelength for Au/CeO_2 and Au/SiO_2 materials that had been functionalized with PATP are shown in Figures 4A and B, respectively. The spectra contain two sets of bands: (i) the signals at 1081, 1142, 1390, 1433 and 1575 cm^{-1} that can be assigned to the A_g modes of DMAB; and (ii) the signals at 1081, 1489 and 1593 cm^{-1} that can be assigned to the A_1 modes of PATP.[48] The PATP conversion can be monitored from the 1433:1081 cm^{-1} DMAB:(PATP+DMAB) intensity ratios, which are depicted in Figure 4C. Our results indicated that the PATP conversion for the Au/CeO_2 material was higher than for Au/SiO_2 under all laser powers. For example, it was around 3-fold higher than for Au/SiO_2 material when the laser-power corresponded to 0.9 mW. It is important to note that an increase in PATP conversion as a function of laser-power irradiation was detected. This observation agrees with the SPR-mediated mechanism for DMAB formation.[49–51] Moreover, no PATP signals were detected when the pure CeO_2 and SiO_2 oxides were employed as substrates.

We also investigate the laser-wavelength-dependence in the PATP conversion. Lower PATP conversions were detected at 785 nm relative to 633 nm (Figure 4D), even though the

View Article Online
DOI: 10.1039/C8NR00934A

laser intensity employed at 785 nm was higher. This is in agreement with the stronger SPR excitation at 633 nm as a result of the better matching between incoming wavelength and SPR excitation positions.[52]

We would like to propose that the higher performances observed for Au/CeO_2 relative to Au/SiO_2 is associated with the presence of reactive oxygen species at the metal-support interface. These species can be, in addition to atmospheric O_2, be activated by the SPR excitation and thus leading to increased PATP conversions. By using this assumption, it can be observed that the active oxygen species that are present as a result of the metal support interactions contribute with 54, 37, 65, and 68% of the activities towards PATP conversion when the laser power corresponded to 0.01, 0.08, 0.38, and 0.90 mW, for example. Surprisingly, this result demonstrates that, for oxidations promoted by activated O_2, metal-support interactions can not only be put to work towards the optimization of SPR-mediated transformations, but also can play an even more important role towards the detected performances relative to atmospheric O_2. This is especially attractive in the context of the utilization of plasmonics towards green catalytic oxidations under ambient conditions.

It is important to note that the SPR wavelength for the Au/CeO_2 NPs is shifted to 540 nm relative to 520 nm in the Au/SiO_2 sample (Figure 1C). This red shift could improve the resonance between SPR frequency and the wavelength of the excitation source, and thus lead to higher PATP conversion for the Au/CeO_2 sample relative to Au/SiO_2. However, we believe that this effect does not play the major role over the detected activities. We propose that the major contribution for the detected activities comes from the activation of oxygen species from CeO_2. In order to further support this hypothesis, we prepared Au NPs supported on TiO_2 and ZrO_2. These samples display SPR wavelengths that are red-shifted relative to Au/SiO_2 and on similar spectral positions as compared to Au/CeO_2 (Figure S6A). Despite the red-shifted SPR

View Article Online
DOI: 10.1039/C8NR00934A

positions, both Au/TiO_2 and Au/ZrO_2 samples displayed PATP conversions that were similar to Au/SiO_2 and much lower relative to Au/CeO_2 (Figure S6B).

We also probed the catalytic activity of Au/CeO_2 and Au/SiO_2 towards the oxidation of aniline driven by visible-light under ambient conditions (room temperature, 1 atm of O_2 or N_2, and employing a 300 W tungsten lamp as the excitation source). Figure 5 shows the conversion (%) for the oxidation of aniline after 12 hours by employing Au/CeO_2 and Au/SiO_2 as catalysts under O_2 (red bars). Interestingly, the utilization of both Au/CeO_2 and Au/SiO_2 led to the selective oxidation of aniline to azobenzene under visible light illumination as confirmed by gas chromatography. The utilization of Au/CeO_2 nanoparticles led to 35 % of conversion after 12 h under O_2 atmosphere. This conversion (%) was significantly higher relative to Au/SiO_2 nanoparticles (25%). The temperature of the reaction mixture at the end of the reaction corresponded to ~35 ^oC and no significant conversion was obtained in the absence of any catalyst or in the presence of the CeO_2 and SiO_2 supports. As all catalytic experiments were carried out using the same loading of Au, the differences in conversion (~10 %) between the Au/CeO_2 and Au/SiO_2 nanoparticles were here attributed to the activation of oxygen species from the metal-support interface. In these conditions, activation of oxygen species from the metal-support interface contributed with 28.6% to the detected conversion percentage. It is important to note that no conversion was detected in the absence of the Au/CeO_2 and Au/SiO_2 (blank reactions). Moreover, experiments without visible-light excitation (dark controls) at 35 ^oC led to 2.0 and 0.5% conversions for Au/CeO_2 and Au/SiO_2, respectively.

These results also agree with the aniline conversion percentages obtained in the absence of atmospheric O_2 (experiments carried out under N_2, blue bars). As expected, no significant conversion was detected for Au/SiO_2 (3.5 %). On the other hand, Au/CeO_2 displayed

View Article Online
DOI: 10.1039/C8NR00934A

a 12 % conversion (the only contribution of catalysis come from oxygen species arising from metal-support interactions).

In order to confirm that the transfer of SPR-excited hot electrons from Au NPs to CeO_2 can take place, we studied the photocurrent response of pure CeO_2 and Au/CeO_2 electrodes in the photoelectrochemical oxygen evolution reaction (electrolyte used was KOH 0.1M, pH 13). The light source used was a white light-emitting diode (LED) lamp with maximum intensity at 565 nm and 0.1W/cm^2 total output power. The electrodes were prepared by a sol-gel method using the spin-coating technique as detailed in the experimental section, which yielded Au/CeO_2 thin films with Au NPs size distribution and SPR similar to those of the powder samples also prepared in this work. Figure S7A shows the chopped light (light/dark) linear sweep voltammetry of pure CeO_2 and Au/CeO_2 electrodes. Whereas CeO_2 electrode remains unresponsive to illumination, the voltammetry scan using the Au/CeO_2 electrode shows a clear anodic photocurrent, which can be assigned to the injection of SPR-excited hot electrons from Au to CeO_2.[23]

CONCLUSIONS

We have demonstrated a facile approach for probing and isolating the relative contribution of oxygen species that originate from metal support interactions over the SPR-mediated catalytic activities. We employed Au/CeO_2 as a model catalyst and oxidations mediated by activated O_2 as model transformations. In this case, our approach consisted of comparing the activities of Au/CeO_2 catalysts (SPR excitation can activate oxygen species from both metal-support interactions and from O_2 atmosphere) relative to Au/SiO_2 (SPR excitation can activate only atmospheric O_2 due the absence of active oxygen species originating from

View Article Online
DOI: 10.1039/C8NR00934A

metal-support interactions) and probing the performances of Au/CeO_2 in the absence of O_2 atmosphere. Surprisingly, we found that the activation of oxygen species from the metal-support interface in Au/CeO_2 can lead to substantial improvements in catalytic activity. Moreover, these species can play, under appropriate conditions, a major role over activities relative to the activation of atmospheric O_2, which is very commonly used as an oxidant in the context of green catalytic transformations. These results provide new insights on the various factors governing plasmonic catalytic activities and can inspire the development of novel optimization strategies for the efficient use of plasmonic effects to drive solar-powered catalytic transformations.

EXPERIMENTAL SECTION

Materials and Instrumentation

Analytical grade hydrogen tetrachloroaurate trihydrate ($HAuCl_4 \cdot 3H_2O$, 48% Au, Sigma-Aldrich), polyvinylpyrrolidone (PVP, Sigma-Aldrich, M_w = 55.000 $g.mol^{-1}$), L-ascorbic acid ($C_6H_8O_6$, ≥ 99.0%, BioXtra, Sigma-Aldrich), *p*-aminothiophenol ($HSC_6H_4NH_2$, > 97%.0%, Sigma-Aldrich), *p*-nitrophenol ($HOC_6H_4NO_2$, > 98%, Merck-Schuchardt), ethanol (C_2H_5OH, Vetec), acetone (C_3H_6O, Sigma-Aldrich), aniline ($C_6H_5NH_2$, Synth), dimethyl sulfoxide (C_2H_6OS, > 99.9%, Sigma-Aldrich), silica (pore size 22nm, 155 m^2g^{-1}, CAS number 112926-00-8, Sigma-Aldrich), titanium oxide (pore size 20 nm, > 30 m^2g^{-1}, CAS number 13463-67-7, Degussa), cerium oxide (pore size < 50 nm, 30 m^2g^{-1}, CAS number 1306-38-3, Sigma-Aldrich), tungsten oxide (pore size < 100 nm, CAS number 1314-35-8, Sigma-Aldrich), and zirconium oxide (pore size < 100 nm, > 25 m^2g^{-1}, CAS number 1314-23-4, Sigma-Aldrich) were used without further purification. Deionized water (18.2 MΩcm) was used throughout the experiments.

View Article Online
DOI: 10.1039/C8NR00934A

The scanning electron microscopy (SEM) images were obtained using a JEOL field emission gun microscope, JSM 6330F, operated at 5 kV. The samples were prepared by drop-casting an aqueous suspension containing the Au nanospheres, Au/oxide hybrids and pure oxides over a commercial silicon wafer, followed by drying under ambient conditions. The average diameter of the Au nanospheres was determined by individually measuring the diameter of 100 nanostructures from the SEM images. The UV-VIS spectra were obtained from aqueous suspensions of the nanostructures with a Shimadzu UV-2600 PC spectrophotometer, using quartz cuvettes (optical path = 1 cm) Diffuse reflectance measurements were conducted in a ISR-2600 Integrating Sphere attachment, from the Au/oxides and oxides solid samples. Raman and SERS spectra were acquired on a Renishaw InVia Raman Microscope equipped with a CCD detector. The laser beam was focused on the sample by using a 50x lens. The experiments were performed under ambient conditions in a back-scattering geometry. The samples were irradiated 632.8 nm (He-Ne, RL633 Renishaw Class 3B) or at 785 nm (Diode Laser, Renishaw) with controlled laser power outputs. All Raman spectra were acquired in a single scan with 10 s accumulation time. Gold content in the catalyst was measured by FAAS analysis, on a Shimadzu AA-6300 spectrophotometer using a Au hollow cathode lamp (Photron). Powder X-ray diffraction (XRD) patterns were recorded in a Rigaku Miniflex diffractometer with Cu Kα radiation (λ = 1.54 Å) at a 2θ range from 10 to 90°, with a step size of 0.02° and acquisition time of 1° min^{-1}. Temperature-programmed reduction with hydrogen (H_2-TPR) was carried out in a Quantachrome ChemBET-Pulsar instrument equipped with a thermal conductivity detector. Typically, 0.05 g of a catalyst was dried with N_2 flow at 125 °C for 1h and then cooled down to room temperature. The TPR profiles were obtained between 50 and 1100 °C in a flow of 10% H_2/N_2, the temperature increasing linearly at a rate of 10 °C min^{-1}. X-ray photoelectron spectra (XPS) were taken with Thermo Scientific K-Alpha

View Article Online
DOI: 10.1039/C8NR00934A

spectrometer using a 72 W monochromated Al Kαsource (*hv* = 1486.6 eV). The X-rays are focused to give a spot size on the sample of 400 µm in diameter. The analyzer is a double focusing 180-degree hemisphere with mean radius of 125 mm. It is run in constant analyzer energy (CAE) mode. The pass energy was set to 200 eV for survey scans and 50 eV for high resolution region scans. All XPS spectra were referenced according to the adventitious C 1s peak (285 eV). All binding energies were referenced to the C 1s core level at 284.8 eV. Fitting of the experimental spectra was carried out using mixed Gaussian/Lorentzian peak shapes employing CasaXPS software. Semiquantitative analysis accounted for a nonlinear Shirley background subtraction.

Synthesis of Au nanospheres (Au NPs)

In a typical synthesis, 6 mL of an aqueous solution containing 35 mg of PVP and 60 mg of ascorbic acid was prepared. This mixture was heated to 90 ˚C for 10 min with magnetic stirring. Then, 1 mL of 3 mM $AuCl_4^-{}_{(aq)}$ was added dropwise with magnetic stirring and the reaction allowed to proceed for 3 h. The obtained Au NPs were washed several times with 1.5 mL of water by successive cycles of centrifugation and removal of the supernatant and re-suspended in water for further use.[53] This procedure was scaled up by 20 folds for the synthesis of Au/CeO_2 and Au/SiO_2 materials.

Synthesis of Au/CeO_2 and Au/SiO_2 materials

The incipient wetness impregnation method was adopted to immobilize the suspension containing the Au NPs obtained in the previous section over the surface of the commercial metal oxides. In a typical procedure, the obtained Au NPs suspension (scaled-up synthesis) was concentrated in 4.5 mL of ethanol (the Au concentration in this suspension

View Article Online
DOI: 10.1039/C8NR00934A

corresponded to 21 mM). This suspension was dropped onto 500 mg of commercial SiO_2 or CeO_2 to obtain 5 wt% in terms of Au. After the addition of *ca*. 0.5 mL of the suspension into the solid (that was placed in a petri dish), the sample was homogenized using a spatula. In order to avoid slurry formation, the solid was heated for 30 min at 120 °C to remove the excess of ethanol. This process was performed until all the suspension was incorporated into the support, and the material was left to dry a furnace kept at 120 °C overnight placed in the petri dish.[54]

Preparation of Raman substrates

The Au/SiO_2 and Au/CeO_2 solids were suspended in 25 µL of H_2O. 25 µL of the resulting suspension was drop-cast onto a 1x1 cm Si(001) surface and dried in air. The sample was then immediately used for the Raman measurements. For SERS measurements, 40 µL of a 1.0 mM ethanolic solution of *p*-aminothiophenol was drop-cast on the corresponding Raman substrates, followed by drying under ambient conditions. All samples were used immediately for SERS measurements after preparation. All spectra were normalized with respect to the Raman band at 1081 cm^{-1} for the ease of comparison.

SPR-mediated oxidation of aniline

50 mg of Au/CeO_2, Au/SiO_2, CeO_2, or SiO_2 were dispersed in 2 mL of DMSO. In a typical experiment, a mixture of aniline (1 mmol), 66 mg of KOH and 2 mL of the suspension containing the catalysts was transferred to a 15 mL round-bottom flask. After this mixture was purged with O_2 or N_2, it was connected to a balloon filled with O_2 or N_2 (1 atm), respectively. This system was kept under stirring for 12 h at room temperature and irradiated with a 300 W halogen tungsten lamp (OSRAM) mounted at 10 cm from the glass reactor. After the reaction

View Article Online
DOI: 10.1039/C8NR00934A

was completed, the products were centrifuged and analyzed by a GC 2010 Plus Shimadzu instrument equipped with a RTx®-5MS capillary column capillary column. GC conditions: injector 260°C; detector: 110°C; pressure: 100 kPa. Column temperature: 80°C, 1°C/min up to 280°C.

Preparation of Electrodes and Photoelectrochemical Characterization

Sample electrodes were prepared by a spin coating technique. Cerium(III) nitrate hexahydrate (Acros Organics, ≥99.5%) and hydrogen tetrachloroaurate(III) (Acros Organic, ACS reagent grade) were dissolved in mixture of acetic acid/water 5:2 V/V in a 1:0.05 and 1:0.10 mol ratio to give 4 cm^3 of a solution with 1 M total metal concentration, which was then diluted with 2 cm^3 2-metoxy-ethanol. The resulting solution was used to spin-coat fluorine-doped tin oxide glass subtracted at 3000 rpm. Prior to coating, the substrates were cleaned by ultrasound rinsing in acetone and then in ethanol for 10 minutes each. After coating, substrates were placed in a furnace pre-heated to 200 °C. As soon as the coated substrate were in the furnace, it was set to 400 °C at a heating rate of 10 °C/min. After 4 hours, the substrates were quenched to room temperature. One coat-annealing cycle was enough to produce continuous films, whose thickness can be controlled by increasing the number of cycles. However, the study presented in this report was done using one-cycle thin films.[23]

The electrolyte was prepared by dissolving 50 mmols potassium hydroxide (Sigma-Aldrich, ≥99.0%) and 200 mmol potassium sulfate (Sigma-Aldrich, ≥99.0%) in 500 mL of distilled water. The sample was placed in a PEC cell with a 3 mm diameter opening. Photoelectrochemical measurement was made using a Zahner Elektrik Impedance Measurement Unit (Model IM6), using a a white light-emitting diode (LED) lamp with maximum intensity at 565 nm and 0.1W/cm2 total output power which was calibrated to

closely resemble the AM1.5 global spectrum at 100 mW/cm^2. For the three-electrode measurements of the CeO_2 and Au-CeO_2 photoanodes, the counter electrode was a Pt wire with excess surface area, and the reference electrode was Ag/AgCl (3M NaCl). Electrochemical potentials were converted to the reversible hydrogen electrode (RHE) scale.

ACKNOWLEDGEMENTS

This work was supported by the Fundação de Amparo à Pesquisa do Estado de São Paulo (FAPESP) (grant numbers 2015/21366-9 and 2015/26308-7). R.S.G. thanks to CAPES for research fellowship. J.Q. thanks São Paulo Research Foundation (FAPESP) grant number 2016/17866-9. C.J.R thanks the CNPq for the fellowship. P.H.C.C. and R.A.A. thank the CNPq for the research fellowships.

REFERENCES

1 S. Linic, U. Aslam, C. Boerigter and M. Morabito, *Nat Mater*, 2015, **14**, 567–576.
2 M. L. Brongersma, N. J. Halas and P. Nordlander, *Nat. Nanotechnol.*, 2015, **10**, 25–34.
3 C. Boerigter, U. Aslam and S. Linic, *ACS Nano*, 2016, **10**, 6108–6115.
4 Z. Zhenyi, H. Jindou, F. Yurui, Z. Mingyi, L. Kuichao and D. Bin, *Adv. Mater.*, 2017, **29**, 1606688.
5 J. Wen, J. Xie, H. Zhang, A. Zhang, Y. Liu, X. Chen and X. Li, *ACS Appl. Mater. Interfaces*, 2017, **9**, 14031–14042.
6 K. Pan-Yong, R. Jing-Run, L. Zhao-Qing, W. Hong-Juan, L. Nan, S. Yu-Zhi, J. Yong-Gang and Q. Shi-Zhang, *Chem. A Eur. J.*, 2015, **21**, 15360–15368.
7 X. Wei, C. Shao, X. Li, N. Lu, K. Wang, Z. Zhang and Y. Liu, *Nanoscale*, 2016, **8**, 11034–11043.
8 Z. Zhenyi, J. Xiaoyi, L. Benkang, G. Lijiao, L. Na, W. Li, H. Jindou, L. Kuichao and D. Bin, *Adv. Mater.*, 2018, **30**, 1705221.
9 K. Pan-Yong, Z. Ping-Xuan, L. Zhao-Qing, L. Jin-Long, W. Hao, L. Nan and M. Tian-Yi, *Small*, 2016, **12**, 6735–6744.
10 U. Aslam, S. Chavez and S. Linic, *Nat. Nanotechnol.*, 2017, **12**, 1000.
11 S. Mukherjee, F. Libisch, N. Large, O. Neumann, L. V. Brown, J. Cheng, J. B. Lassiter, E. A. Carter, P. Nordlander and N. J. Halas, *Nano Lett.*, 2013, **13**, 240–247.
12 P. Christopher, H. Xin and S. Linic, *Nat. Chem.*, 2011, **3**, 467–472.
13 A. Marimuthu, J. Zhang and S. Linic, *Science*, 2013, **339**, 1590–1593.
14 A. G. M. da Silva, T. S. Rodrigues, V. G. Correia, T. V Alves, R. S. Alves, R. A. Ando, F. R.

View Article Online
DOI: 10.1039/C8NR00934A

Ornellas, J. Wang, L. H. Andrade and P. H. C. Camargo, *Angew. Chem. Int. Ed.*, 2016, **55**, 7111–7115.
15 J. Wang, R. A. Ando and P. H. C. Camargo, *Angew. Chem. Int. Ed.*, 2015, 6909-6912.
16 D. Ravelli, M. Fagnoni and A. Albini, *Chem. Soc. Rev.*, 2013, **42**, 97–113.
17 C. Meng, K. Yang, X. Fu and R. Yuan, *ACS Catal.*, 2015, **5**, 3760–3766.
18 A. Tanaka, K. Hashimoto and H. Kominami, *J. Am. Chem. Soc.*, 2012, **134**, 14526–14533.
19 B. Li, B. Zhang, S. Nie, L. Shao and L. Hu, *J. Catal.*, 2017, **348**, 256–264.
20 J. Wang, F. J. Trindade, C. B. De Aquino, J. C. Pieretti, S. H. Domingues, R. A. Ando and P. H. C. Camargo, *Angew. Chem. Int. Ed.*, 2015, 9889–9894.
21 L. Papa, I. C. De Freitas, R. S. Geonmonond, C. B. De Aquino, J. C. Pieretti, S. H. Domingues, R. A. Ando and P. H. C. Camargo, *J. Mater. Chem. A*, 2017, 5, 11720-11729.
22 T. Montini, M. Melchionna, M. Monai and P. Fornasiero, *Chem. Rev.*, 2016, **116**, 5987–6041.
23 H. Jia, X. M. Zhu, R. Jiang and J. Wang, *ACS Appl. Mater. Interfaces*, 2017, **9**, 2560–2571.
24 B. Chen, X. Li, R. Zheng, R. Chen and X. Sun, *J. Mater. Chem. A*, 2017, **5**, 13382–13391.
25 V. A. and R. P. and M. F. and O. M. M. and M. A. Iatì, *J. Phys. Condens. Matter*, 2017, **29**, 203002.
26 J. A. Rodriguez, R. Si, J. Evans, W. Xu, J. C. Hanson, J. Tao and Y. Zhu, *Catal. Today*, 2015, **240**, **Part**, 229–235.
27 L. Pautrot-D'Alençon, P. Barboux and J. P. Boilot, *J. Sol-Gel Sci. Technol.*, 2006, **39**, 261–267.
28 R. Chelikowsky, N. Troullier and E. King, *Phys. Rev. B*, 1991, **44**, 489-497.
29 T. S. Wu, H. D. Li, Y. W. Chen, S. F. Chen, Y. S. Su, C. H. Chu, C. W. Pao, J. F. Lee, C. H. Lai, H. T. Jeng, S. L. Chang and Y. L. Soo, *Sci. Rep.*, 2015, **5**, 15415.
30 D. Andreeva, I. Ivanov, L. Ilieva, J. W. Sobczak, G. Avdeev and T. Tabakova, *Appl. Catal. A Gen.*, 2007, **333**, 153–160.
31 A. H. M. da Silva, T. S. Rodrigues, A. G. M. da Silva, P. H. C. Camargo, J. F. Gomes and J. M. Assaf, *J. Mater. Sci.*, 2017, 52, 13764-13778.
32 A. G. M. Silva, T. S. Rodrigues, A. Dias, H. V Fajardo, R. F. Goncalves, M. Godinho and P. A. Robles-Dutenhefner, *Catal. Sci. Technol.*, 2014, **4**, 814–821.
33 S. Mandal, K. K. Bando, C. Santra, S. Maity, O. O. James, D. Mehta and B. Chowdhury, *Appl. Catal. A-General*, 2013, **452**, 94–104.
34 J. Li, X. Liu, W. Zhan, Y. Guo, Y. Guo and G. Lu, *Catal. Sci. Technol.*, 2016, **6**, 897–907.
35 A. Nakajima, A. Yoshihara and M. Ishigame, *Phys. Rev. B*, 1994, **50**, 13297–13307.
36 S.-Y. Chen, R.-J. Chen, W. Lee, C.-L. Dong and A. Gloter, *Phys. Chem. Chem. Phys.*, 2014, **16**, 3274.
37 C. M. Kalamaras, K. Petallidou and A. M. Efstathiou, *Appl. Catal. B.,* 2013, **143**, 225-238.
38 X. Liu, K. Zhou, L. Wang, B. Wang, Y. Li, *J. Am. Chem. Soc.,* 2009, *131*, 3140–3141.
39 M. M. Natile, G. Boccaletti and A. Glisenti, *Chem. Mater.*, 2005, **17**, 6272–6286.
40 J.-D. Grunwaldt, C. Kiener, C. Wögerbauer and A. Baiker, *J. Catal.*, 1999, **181**, 223–232.
41 J. Quiroz, J.-M. Giraudon, A. Gervasini, C. Dujardin, C. Lancelot, M. Trentesaux and J.-F. Lamonier, *ACS Catal.*, 2015, **5**, 2260–2269.
42 M. Setvin, U. Aschauer, P. Scheiber, Y.-F. Li, W. Hou, M. Schmid, A. Selloni and U.

View Article Online
DOI: 10.1039/C8NR00934A

Diebold, *Science*, 2013, **341**, 988–991.
43 M. E. Stewart, C. R. Anderton, L. B. Thompson, J. Maria, S. K. Gray, J. A. Rogers and R. G. Nuzzo, *Chem. Rev.*, 2008, **108**, 494–521.
44 N. Jiang, X. Zhuo and J. Wang, *Chem. Rev.*, 2017, **118**, 3054-3099.
45 L. Bin Zhao, M. Zhang, Y. F. Huang, C. T. Williams, D. Y. Wu, B. Ren and Z. Q. Tian, *J. Phys. Chem. Lett.*, 2014, **5**, 1259–1266.
46 J. Chu, P. Miao, X. Han, Y. Du, X. Wang, B. Song and P. Xu, *ChemCatChem*, 2016, **8**, 1819–1824.
47 X. Hu, T. Wang, L. Wang and S. Dong, *J. Phys. Chem. C*, 2007, **111**, 6962–6969.
48 Y. Fang, Y. Li, H. Xu and M. Sun, *Langmuir*, 2010, **26**, 7737–7746.
49 S. Wu, J. Wang, P. Song and L. Xia, *Plasmonics*, 2016, 611–620.
50 Y. F. Huang, M. Zhang, L. Bin Zhao, J. M. Feng, D. Y. Wu, B. Ren and Z. Q. Tian, *Angew. Chem. Int. Ed.*, 2014, **53**, 2353–2357.
51 J. L. Wang, R. A. Ando and P. H. C. Camargo, *ACS Catal.*, 2014, **4**, 3815–3819.
52 W. Hermoso, T. V. Alves, C. C. S. De Oliveira, E. G. Moriya, F. R. Ornellas and P. H. C. Camargo, *Chem. Phys.*, 2013, **423**, 142–150.
53 T. C. Damato, C. C. S. de Oliveira, R. A. Ando and P. H. C. Camargo, *Langmuir*, 2013, **29**, 1642–1649.
54 L. Ma, I. Jia, X. Guo and L. Xiang, *Chinese J. Catal.*, 2014, **35**, 108–119.

View Article Online
DOI: 10.1039/C8NR00934A

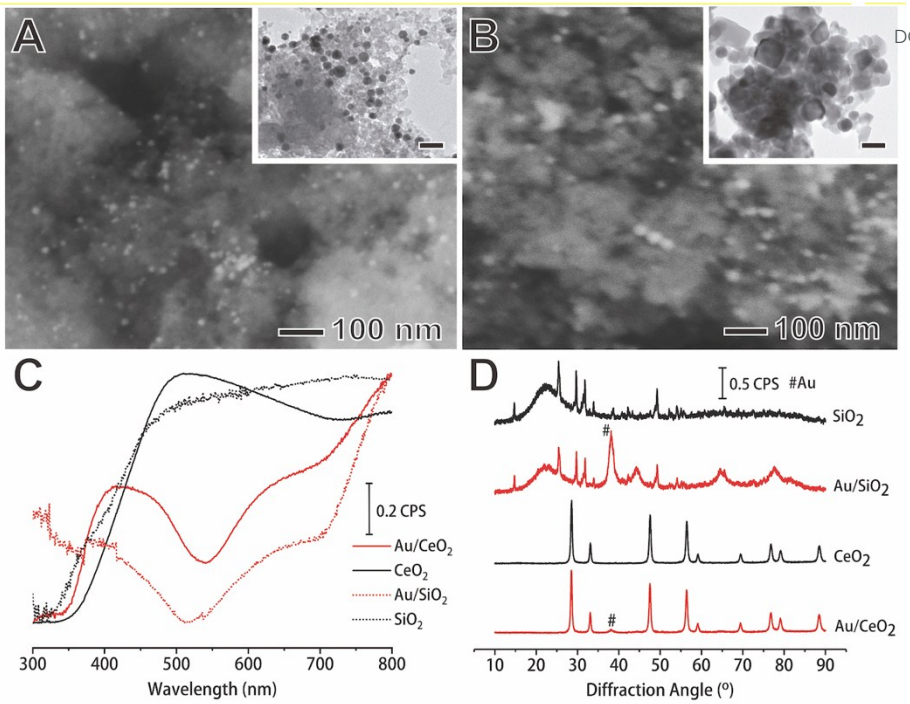

Figure 1. SEM and TEM (insets) images for (A) Au/SiO_2 and (B) Au/CeO_2 materials. The scale bars in the insets correspond to 100 nm. (C) Diffuse reflectance spectra for Au/CeO_2, CeO_2, Au/SiO_2 and SiO_2 (solid red, solid black, dashed red and dashed black lines, respectively). (D) X-ray diffraction patterns for SiO_2, Au/SiO_2, CeO_2 and Au/CeO_2 (top to bottom traces, respectively).

View Article Online
DOI: 10.1039/C8NR00934A

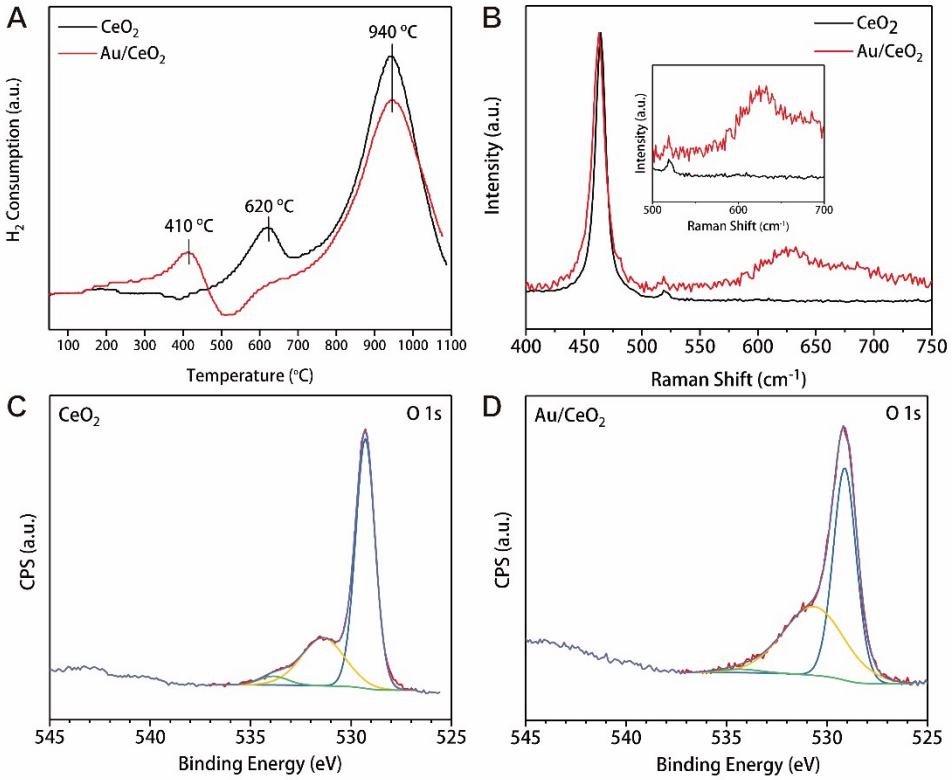

Figure 2. (A) Temperature programmed reduction profiles for CeO_2 and Au/CeO_2 materials (black and red lines, respectively). (B) Raman spectra of CeO_2 and Au/CeO_2 materials (black and red lines, respectively). All spectra were recorded under 632.8 nm with an exposure time of 20 s. (C and D) Deconvoluted XPS spectra of the O 1s core level for CeO_2 (C) and Au/CeO_2 (D).

View Article Online
DOI: 10.1039/C8NR00934A

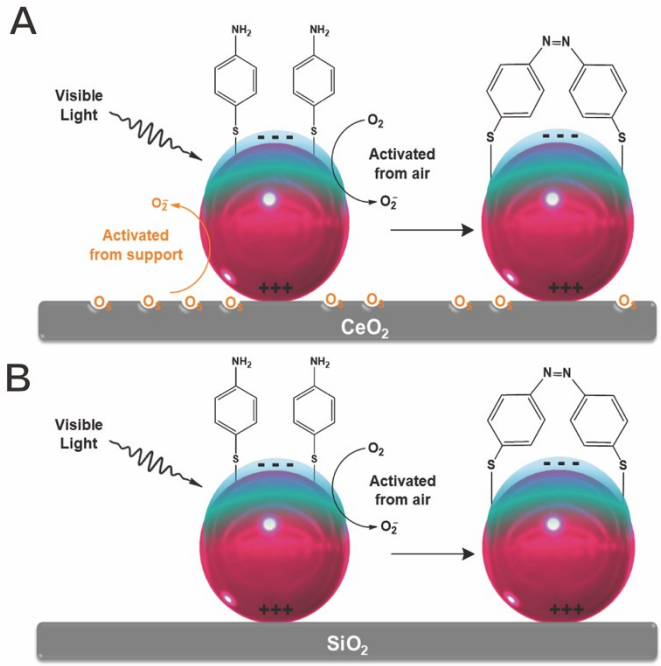

Figure 3. Scheme for the SPR-mediated oxidation of PATP to DMAB promoted by activated oxygen under visible light employing Au/CeO_2 and Au/SiO_2 as substrates. In Au/CeO_2 (A), the activation of atmospheric oxygen (O_2 black trace) and surface oxygen species (O_S, orange trace) take place and contribute to the PATP to DMAB conversion. In Au/SiO_2 (B), only the activation of atmospheric oxygen takes place.

View Article Online
DOI: 10.1039/C8NR00934A

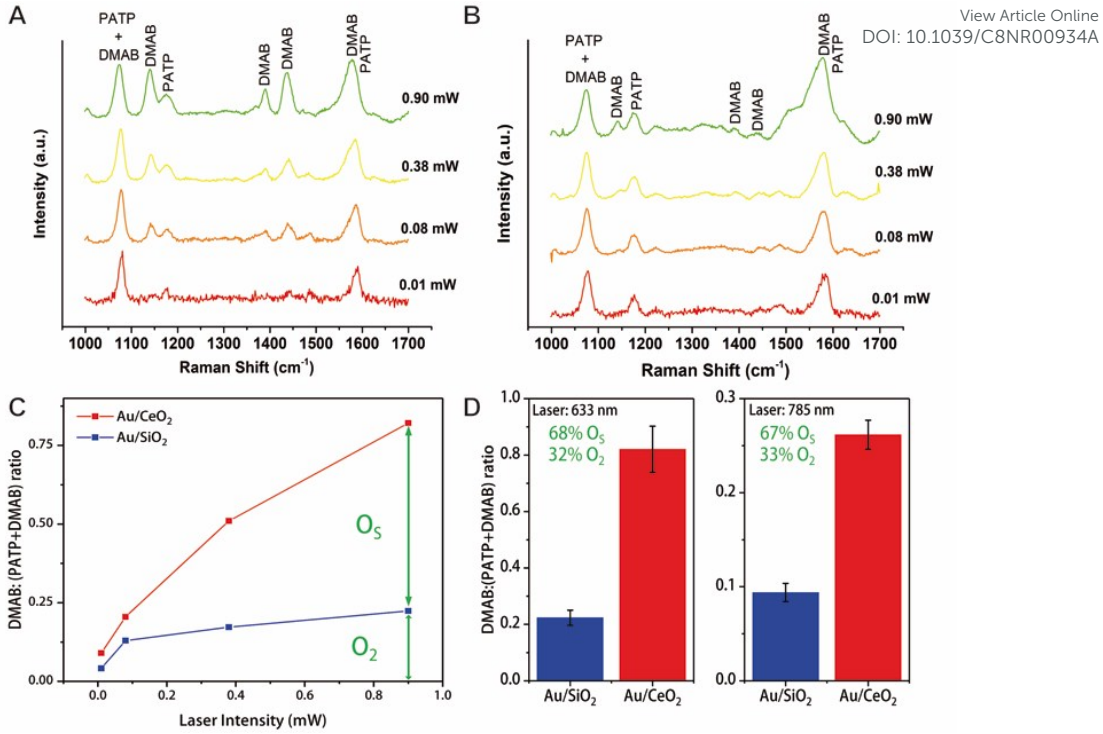

Figure 4. Laser-power-dependent SERS spectra for (A) Au/CeO_2 and (B) Au/SiO_2 materials that had been functionalized with PATP at 0.01, 0.08, 0.38 and 0.90 mW with an exposure time of 10 s. All spectra were recorded employing 632.8 nm as the excitation wavelength and were normalized with respect to the band at 1081 cm^{-1}. (C and D) Laser-power-dependent (C) and laser-wavelength-dependent (D) oxidation of PATP, expressed as the DMAB:(PATP+DMAB) ratio, for Au/CeO_2 and Au/SiO_2 (red and blue lines/bars, respectively).

View Article Online
DOI: 10.1039/C8NR00934A

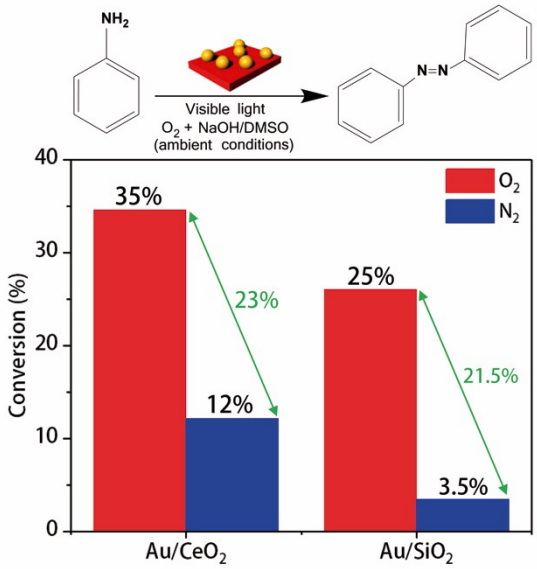

Figure 5. Oxidation of aniline catalyzed by Au/CeO_2 and Au/SiO_2 materials under O_2 and N_2 atmospheres (red and blue bars, respectively). Conversion % are expressed for 12 h of reaction time. The reaction was carried out under ambient conditions and employing DMSO as the solvent. The Au loading corresponded to 4.2 %wt in all cases.

View Article Online
DOI: 10.1039/C8NR00934A

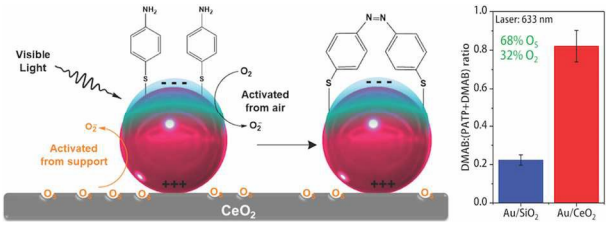

This paper unravels the contribution from active surface oxide species at the metal-support interface over activities in SPR-mediated oxidation reactions.